Earth and Planetary Science Letters 580 (2022) 117363

Contents lists available at ScienceDirect

Earth and Planetary Science Letters

www.elsevier.com/locate/epsl

Transitions in subduction zone properties align with long-term topographic growth (Cascadia, USA)

Lorenz Michel-Wolf [a], Todd A. Ehlers [a,*], Rebecca Bendick [b]

[a] Department of Geosciences, University of Tübingen, Tübingen, Germany
[b] Department of Geosciences, University of Montana, Missoula, MT, USA

ARTICLE INFO

Article history:
Received 14 June 2021
Received in revised form 22 September 2021
Accepted 30 December 2021
Available online 24 January 2022
Editor: A. Webb

Keywords:
subduction zone
long-term deformation
thermochronometry
seismic cycle
mechanics

ABSTRACT

Simple mechanical models of the earthquake cycle assume that interseismic elastic deformation is recovered during earthquakes, closing the strain budget of steady and episodic slip on the deep and shallow subduction interfaces, respectively. However, elevated topography in the forearc high requires that some deformation is not recovered over each elastic cycle. Here, we compare constraints on deformation over decadal to million-year timescales to disentangle contributions from elastic (recoverable) and inelastic (unrecoverable) deformation within the Olympic Mountains of the Cascadia Subduction Zone. Over timescales of 10^3 – 10^6 yrs, elevated topography, permanent deformation, and denudation (from thermochronometry and cosmogenic nuclide data) accumulate in an area adjacent, but not identical, to the maximum in geodetically observed reduced vertical velocity and surface upwarping over tens of years. The domains of geodetic and geomorphic maximum uplift occur over a 20-60 km wide zone overlying the up-dip limits of the zone of conditional frictional stability at the subduction interface. We attribute geologic-scale orogenesis, accumulation of topography and advection of rocks in the active orogen to unrecoverable deformation as stress is relayed up-dip through parts of the subduction interface and dissipated in the overriding plate.

1. Introduction

The development of mountain topography (corresponding to surface uplift) requires the accumulation of permanent tectonic deformation (through rock uplift) at a rate greater than, or equal to that at which denudation removes topography over geologic timescales (Ellis et al., 1999; Melnick, 2016). In the case that mountain topography is in steady state and no surface uplift occurs, rock uplift equals denudation and the respective measures can be compared with each other (England and Molnar, 1990). Rock uplift is commonly determined by geodetic methods (see England and Molnar, 1990), whereas denudation and rock exhumation are often calculated with thermochronometry and cosmogenic radionuclide methods. Despite decades of research related to quantifying orogen deformation and exhumation processes, we still lack a clear understanding of the relationship between elastic (recoverable) and permanent deformation over separated short (e.g., $\sim 10^0$–10^2 yrs.) and longer (e.g., 10^3–10^7 yrs.) time scales. This shortcoming is exacerbated by recent advances in understanding of the mechanics of fault interfaces, with pronounced differences in the accommodation of deformation between footwall and hanging wall, especially in the dip direction.

At subduction zones, observed surface deformation (on timescales of 10^0–10^2 years) corresponds mostly to elastic strain accumulated during the interseismic period between major earthquakes on the shallow parts of the subduction interface that is frictionally locked. However, mechanical models of more complex time-dependent deformation have recently evolved from simple models of the elastic earthquake cycle on a locked or steadily creeping fault interface (e.g., Mansinha and Smylie, 1971; McCaffrey et al., 2007; Okada, 1985). In particular, recent work on fault mechanics and nonlinear friction combined with direct observations of tectonic motion demonstrates that subduction interfaces have locked domains, freely slipping domains, and transitional domains that host complicated and spatially heterogeneous sequences of stick and slip (e.g., Bürgmann, 2018; Lay et al., 2012). Furthermore, the width and distribution of the respective domains affects the shear force at the plate interface, which is critical in controlling the mountain height at convergent plate margins (e.g., Dielforder et al., 2020; Dielforder and Hampel, 2021; Madella and Ehlers, 2021).

In Cascadia (USA) and Japan, the domains of the plate interface are arranged mostly sequentially in the dip direction so that the

* Corresponding author.
E-mail address: todd.ehlers@uni-tuebingen.de (T.A. Ehlers).

https://doi.org/10.1016/j.epsl.2021.117363

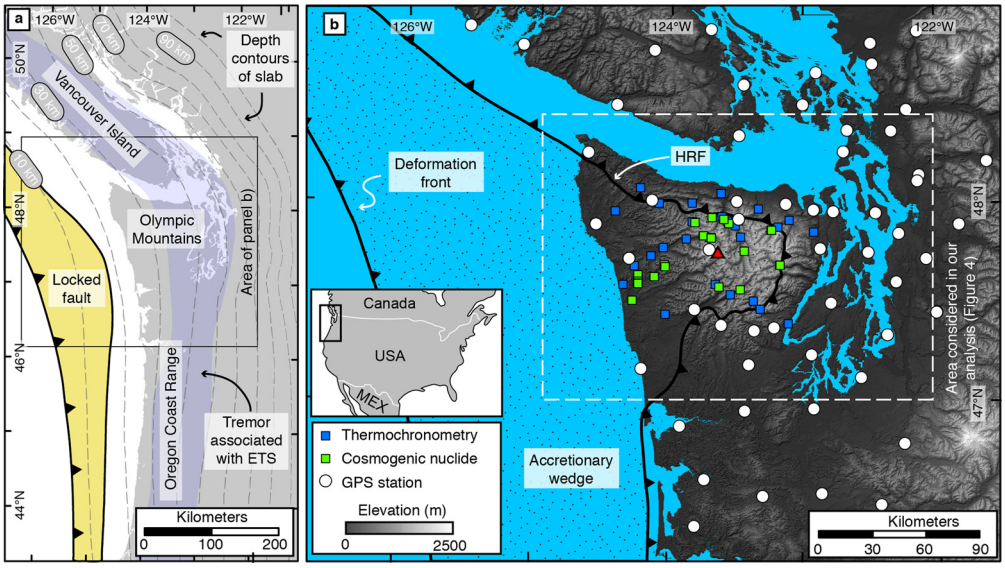

Fig. 1. Overview of the Cascadia Subduction Zone and the Olympic Peninsula of North America. **a)** Map of Cascadia Subduction Zone with depth to the top of the subducting slab indicated by dashed contours from McCrory et al. (2012). Gray is land. The extent of locking of the thrust fault is indicated by the yellow area following Hyndman and Wang (1993). The extent of tremor associated with episodic tremor and slip (ETS) is based on data from the Pacific Northwest Seismic Network (https://pnsn.org/tremor). **b)** Topography of the Olympic Mountains (red triangle indicates Mt. Olympus, 2430 masl), location of GPS stations (data used in this study), and the location of thermochronometry and cosmogenic nuclide samples (Adams and Ehlers, 2018; Michel et al., 2018). The white box denotes the area considered for comparing the different datasets in Fig. 4. The locations of GPS stations used by Bruhat and Segall (2016) for identifying slow slip events are mostly identical with our GPS stations used in our analysis. Labeled maps with thermochronometric cooling ages, denudation rates from cosmogenic nuclides, exhumation rates, and GPS velocities are provided in Figs. 2 and 3, respectively. Onshore location of the Hurricane Ridge Fault (HRF) is after Brandon et al. (1998). (For interpretation of the colors in the figure(s), the reader is referred to the web version of this article.)

shallowest part of the fault interface is locked, sometimes followed by a deeper enigmatic 'gap' zone, then a zone of conditional frictional stability hosting periodically recurring episodic tremor and slip (ETS, Rogers and Dragert, 2003), and finally a steadily slipping zone (Bruhat and Segall, 2016; Wang and Tréhu, 2016). However, how the spatial extents of these zones change over long-time scales (millennial to million years), or even within the earthquake cycle, is not well known, nor is the relationship of recoverable (elastic) strain to permanent strain that leads to the formation of topography in this heterogeneous context.

Here we investigate: (1) the accumulation of permanent deformation and topography over multiple timescales, and (2) how the observed surface deformation maps to the different domains of the subduction interface below. We use the Olympic Mountains, overlying the Cascadia Subduction Zone, Western North America (Fig. 1), as a case study of the spatial and temporal variability of fault slip mechanisms. For our purpose, we compare observations of the position and magnitude of instantaneous vertical displacement from GPS time series with denudation rates derived from cosmogenic nuclide dating and thermochronometry (Adams and Ehlers, 2018; Brandon et al., 1998; Michel et al., 2019, 2018). We further compare these observations with vertical displacement related to ETS and inversions for shear stress on the subduction interface from Bruhat and Segall (2016).

2. Methods

2.1. Data comparison

We compare four different observational data sets with each other. These include three published data sets: Denudation rate data from thermochronometry and cosmogenic nuclides, and vertical displacement due to ETS recorded by GPS. In addition, we calculated new GPS-derived reduced rock uplift rates. Map view figures of the datasets are provided in Fig. 2 and 3, respectively. For a direct comparison of magnitude, spatial scaling, and spatial alignment among the datasets, we project them along a transect crossing the Olympic Peninsula from west to east between -125°E and -122°E (Fig. 4). However, the spatial extent of the datasets differs, and the data based on geodetic observations (Fig. 3) cover a larger area of the Cascadia Subduction Zone compared to estimates of denudation (Fig. 2). To minimize the effects of the bent slab and the variable spatial coverage of the different datasets, we focus our analysis on the area between latitudes 47°N and 48.5°N (dashed white box Fig. 1b; Fig. 4).

2.2. GPS data and processing

We calculated the reduced vertical displacement and velocity from raw GPS observations in a multi-step process. In this study, we define the *reduced vertical displacement* as the epochal change in geodetically-observed vertical position, and *reduced vertical velocity* (or rate) as the linear change of displacement over time after seasonal and interseismic tectonic elastic contributions are removed. The reduced verticals should therefore be dominated by the persistent (unrecoverable) surface displacements that contribute to the growth of topography by the advection of mass.

To calculate the reduced vertical displacement time series, we first solve for the daily positions of 88 continuously logging GPS stations from open data available in the UNAVCO data archive. The stations used include 63 in the Cascadia region and 15 elsewhere. Daily positions were determined for every day and for fortnightly averages from 1 January 2005 to 31 December 2016 using a Kalman filter approach implemented in the GAMIT/GLOBK processing package and tied to the ITRF08 (International Terrestrial Reference Frame, 2008 realization) reference frame using the 15 IGS (International GPS Service) sites outside of the study area. Outlier positions were manually edited, and Markov noise added to the time series using the station position variance and cross-correlations. These are standard GPS processing techniques (e.g., Herring et al., 2016).

Next, because vertical geodetic displacements are sensitive to many different loads, especially hydrologic and seasonal atmospheric masses, the daily vertical (UP) position time series with

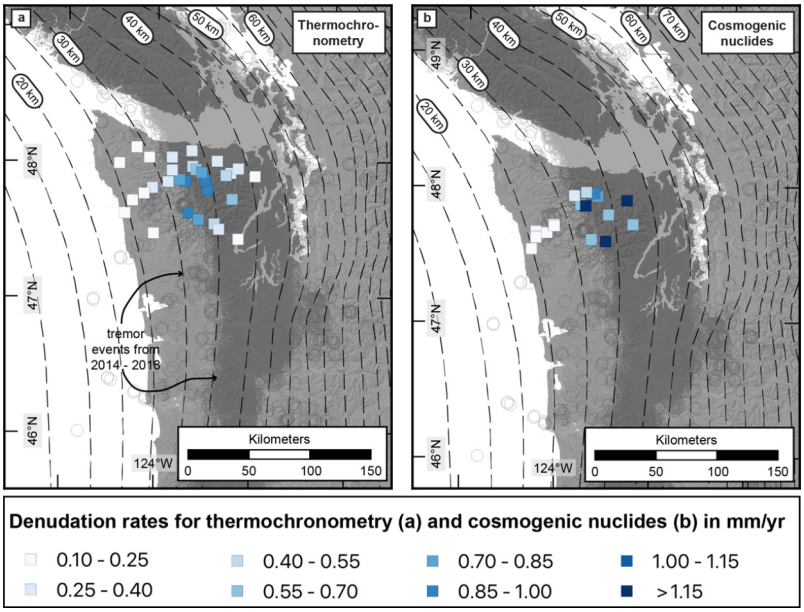

Fig. 2. Denudation rates considered in this study. **a)** Denudation rates obtained from thermo-kinematic modeling of thermochronologic cooling ages at the respective sample sites (Michel et al., 2018). For the full pattern of denudation rates see Fig. S1. **b)** Catchment-wide denudation rates based on cosmogenic nuclide dating (Adams and Ehlers, 2018). Data presented in all subpanels include the depth to the top of the subducted slab (white dashed lines; from McCrory et al., 2012) and the spatial occurrence of tremor events from 2014 – 2018 (dark grey circles or dark grey area), which is based on data from the Pacific Northwest Seismic Network (https://pnsn.org/tremor).

formal uncertainties were used to estimate independent annual sine and cosine harmonics, semiannual sine and cosine harmonics, and secular linear up velocities. The periodic terms together include the seasonal hydrologic and atmospheric contributions, contributions from the GPS satellite orbits (i.e., the draconitic and orbital residuals), and the elastic component (e.g., Bartlow et al., 2011) of the ETS contribution. The steady linear rate (**W**) with these periodic terms removed is therefore the best geodetic estimate of steady decadal mean rock uplift in the late interseismic part of the earthquake cycle (Fig. 3a, Fig. 4d, supplementary Table S2). We note that the elastic contribution from ETS to deformation has an approximately semi-annual recurrence interval, and is removed from the GPS signal through the applied periodic filters.

Furthermore, the station vertical velocity (**W**) is a linear combination of an elastic part due to tectonic loading on the locked part of the Cascadia subduction zone and a residual part due to permanent deformation of the domain. To estimate the reduced vertical rate, we subtract the forward-modeled elastic bending (Fig. 3b) due to the locked subduction zone from Wang et al. (2003) to give the reduced vertical displacement (Fig. 4e, Fig. 3c). Although more recent inversions for horizontal surface velocities incorporate spatially heterogeneous coupling and locking depths on the Cascadia interface, these differ from the earlier purely elastic model in their modeled surface velocities only in the offshore part of the subduction zone (e.g., Li et al., 2018), outside of our study area. Because the study area is well inland of the bottom of the inferred locked zone, the elastic correction is very smooth across the study area (Fig. 3b) regardless of the coupling model used.

In addition to the calculation of the reduced vertical rate, we also calculated the tilting rate. Basic continuum mechanics (e.g., Turcotte and Schubert, 2014) demonstrates that the horizontal spatial derivative of the smoothed GPS reduced vertical positions and velocities can be used to quantify the slope ($\frac{\partial z}{\partial x}$), and topographic tilt or rotation rate (dashed line in Fig. 4e). Since **W** (the vertical velocity) is $\frac{\partial z}{\partial t}$, the x-derivative (section-parallel) of $\mathbf{W}\frac{\partial z}{\partial x \partial t}$ was calculated to determine the topographic tilting rate.

Finally, we note that the Olympic Mountains were glaciated during the last glacial maximum, and continental ice was located to the east and north of the range. The reduced rates reported here are not corrected for glacial isostatic rebound, but based on previous work the magnitude of glacial isostatic rebound is between 0.1-0.3 mm/yr on the Olympic Peninsula (James et al., 2009; Yousefi et al., 2020). Therefore, it is a small component of the rock uplift interpreted here, and the regional postglacial correction is linear across the entire study region and cannot be the source of the observed short-wavelength velocity gradients discussed later. Contributions from multi-year drought (e.g., Fu et al., 2015) are similarly smooth across the study area.

3. Observations from previously published work

3.1. The Olympic Mountains as part of the Cascadia subduction zone

The Cascadia Subduction Zone (CSZ), where the Juan de Fuca Plate subducts below North America, extends along the west coast from northern California to the northern tip of Vancouver Island (Fig. 1a). The Olympic Mountains correspond to the subaerially exposed part of the subduction zone's accretionary wedge (Brandon et al., 1998). Based on thermochronometer cooling ages, cooling histories of rocks collected at the Earth's surface can be reconstructed, and by modeling the temporal evolution of the geothermal gradient, exhumation histories can be reconstructed from sample cooling histories. In the Olympic Mountains, exhumation is localized into a circular-shaped pattern (Brandon et al., 1998; Michel et al., 2019, 2018; see Figure S1), which is a consequence of the syntaxial bend in the subducted slab (e.g., Bendick and Ehlers, 2014; Koptev et al., 2019; Nettesheim et al., 2018). Anomalous exhumation is bounded along strike because of the 3D topology of the down-going Juan de Fuca slab (Hayes et al., 2018). Results from topographic analyses and denudation rates derived from cosmogenic nuclides also corroborate that the evolution of this mountain range is mostly controlled by the shape of the subducted slab (Adams and Ehlers, 2018, 2017). At the latitude of the Olympic Mountains (which form the topographic apex of the forearc high of the subduction zone), the locked zone of the fault is inferred to be wider than farther to the north and south (Fig. 1a) due to the lower angle of subduction below the mountain range (Hyndman, 2013; McCrory et al., 2012; Wang and Tréhu, 2016). The last

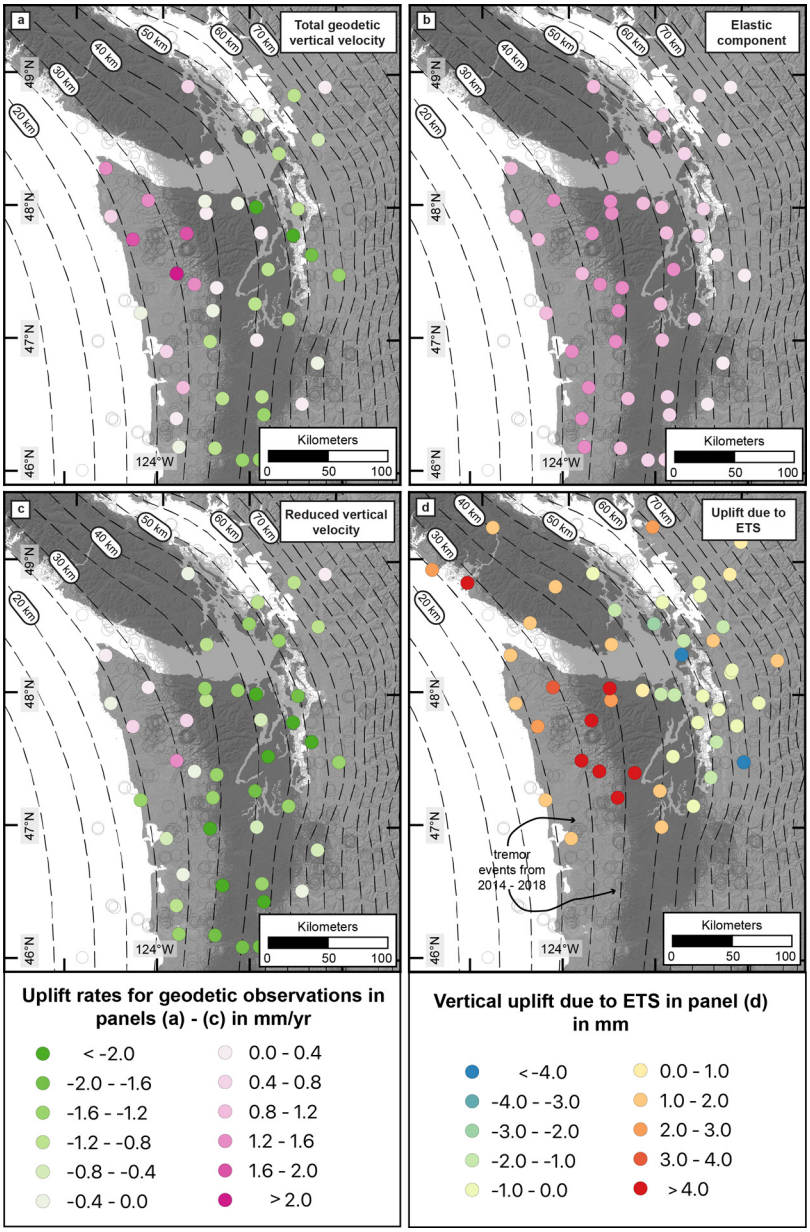

Fig. 3. Maps of the location of GPS stations considered in this study and the respective velocities. a) Rock uplift rates for GPS stations reported in this study. The rates correspond to the total, vertical geodetic velocity, and are not corrected for the elastic component. **b)** Values for the elastic component calculated at the respective location of the GPS station using the model of Wang et al. (2003). **c)** Reduced vertical GPS velocities, derived by subtracting the elastic component (in b) from the rock uplift rates in a). **d)** Rock uplift due to episodic tremor and slip (ETS) as reported by Bruhat and Segall (2016). The observed displacement corresponds to the average displacement from eight events recorded between 2000–2015. Data presented in all subpanels include the depth to the top of the subducted slab (white dashed lines; from McCrory et al., 2012) and the spatial occurrence of tremor events from 2014–2018 (dark grey circles or dark grey area), which is based on data from the Pacific Northwest Seismic Network (https://pnsn.org/tremor).

known complete rupture of the subduction interface occurred in AD 1700 (Wang and Tréhu, 2016).

3.2. Observed Cascadia subduction zone exhumation and deformation mechanics

Several geodetic studies near the CSZ assume all observed displacement to be elastic (e.g., Burgette et al., 2009; McCaffrey, 2009; Szeliga et al., 2008) based on a limiting model of accumulated elastic strain during interseismic periods of the earthquake cycle that is recovered coseismically during slip on the thrust fault (e.g., Hyndman and Wang, 1993). However, this assumption of elastic and fully recoverable deformation is contradictory to several observations: the presence of topography (i.e., the fore arc high / Olympic Mountains); discrepancies between rock uplift rates integrating over different timescales (Kelsey et al., 1994; Penserini et al., 2017); and results from modeling studies (Simpson, 2015; Wang et al., 2003; Wang and Tréhu, 2016).

Even mechanical solutions that incorporate realistic viscoelastic material properties simplify the transition from a freely slipping to a locked subduction interface (e.g., Li et al., 2015; Wang et al., 2003), usually as a fixed line at a discrete 'locking depth'. However, inversions of geodetic and seismic observations from the Cascadia megathrust propose a more complicated pattern (see Fig. 1a and Fig. 4a), with locked conditions from the trench to depths of ~16 km (Krogstad et al., 2016) or 21 km (Bruhat and Segall, 2016), then an inferred velocity-strengthening 'gap' zone where shear stress decreases over time (Bruhat and Segall, 2016). Further

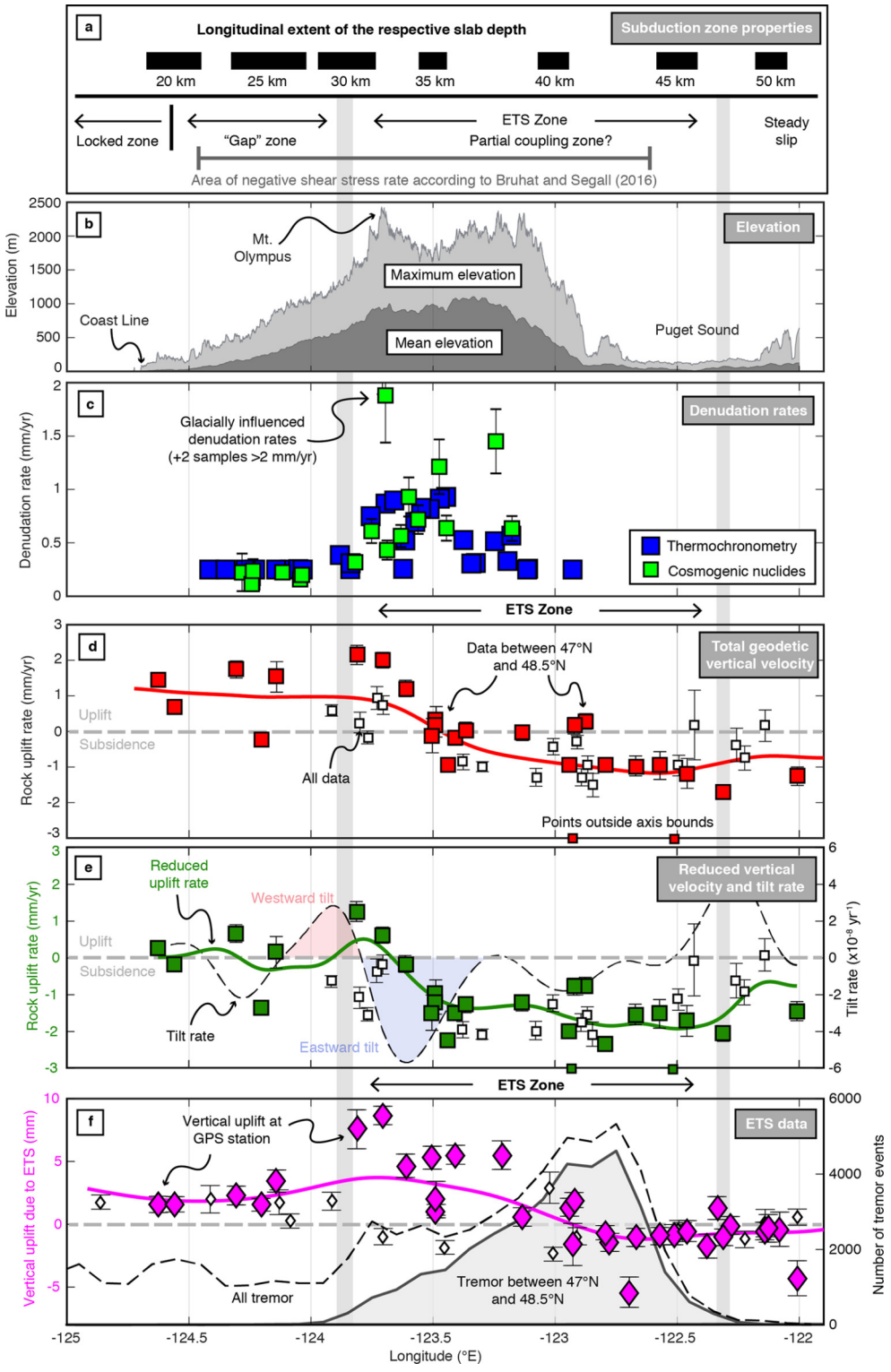

Fig. 4. West to east transects across the Olympic Peninsula, comparing the datasets considered in our analysis. Solid symbols indicate data from the focus study area between 47°N and 48.5°N (white box in Fig. 1b). For completeness, the open, small symbols in panels d) to f) show other data outside the focus area. The solid lines displayed in panels d) to f) were fit using all available data. **a)** The black bars indicate the longitudinal extent of the subducted slab at depth, according to McCrory et al. (2012). Because the slab is curved, the same slab depth can be found at different longitudes along strike of the subduction zone (the wider the bar, the stronger the curvature). The different zones at the subduction zone interface are indicated at the bottom. **b)** Mean and maximum elevation of the central Olympic Peninsula between latitudes of 47.4°N and 48.1°N. **c)** Estimates of denudation rates, based on cosmogenic nuclide dating (Adams and Ehlers, 2018; green squares) and thermochronometry (Michel et al., 2018; blue squares). **d)** Total, vertical GPS velocities used in this study taken from the UNAVCO data archive and treated as outlined in the methods section. **e)** Reduced vertical GPS velocities (green symbols) were obtained from the GPS velocities by subtracting a forward modeled elastic component (Fig. 3b) using the model of Wang et al. (2003). The tilt rate (dashed black line) corresponds to the derivative of the reduced vertical velocity (solid green line) in the x-direction and has units of 10^{-8} yr^{-1}. The areas experiencing westward or eastward surface tilting related to visco-plastic flow are indicated. **f)** Data related to episodic tremor and slip (ETS), showing the vertical uplift due to ETS recorded by GPS stations (Bruhat and Segall, 2016). Tremor events (between 2014–2018) are taken from the tremor database of the Pacific Northwest Seismic Network (https://pnsn.org/tremor) and are grouped in number of events per bins of 0.1° width. We consider events between 47°N and 48.5°N (shaded region) because the occurrence of tremor follows the bent shape of the subducted slab (Fig. 1a).

down-dip the plate interface, a zone of conditional friction hosting episodic tremor and slip (ETS) is inferred from ~25–60 km (Bartlow et al., 2011; Dragert and Wang, 2011; Hawthorne and Rubin, 2013; Wech and Bartlow, 2014). Finally, below the ETS zone, the CSZ slips steadily at the relative plate velocity. These results all point toward complex zones over which tectonic stresses may be stored as elastic potential, dissipated by aseismic viscous flow, or transferred along the subduction interface over time.

3.3. Observed topography and rates of rock uplift and denudation

Two of the published data sets (Adams and Ehlers, 2018; Michel et al., 2018) considered here are sensitive to denudation and include cosmogenic nuclide measurements of ^{10}Be and apatite and zircon (U-Th)/He thermochronometry. These datasets have integration timescales of 10^3–10^4 or 10^5–10^6 years, respectively, and integrate over many seismic cycles to yield a proxy for denudation associated with long-term deformation. Rates obtained from cosmogenic nuclides provide basin-wide denudation rates (Fig. 2b) and are plotted at the respective sample site within the transect (green symbols in Fig. 4c). Previous work by Michel et al. (2018) suggested a circular pattern of denudation, obtained from thermo-kinematic modeling of thermochronometry data (Fig. S1). Here we extract the model-derived denudation rates of Michel et al. (2018) at the respective thermochronometer sample location and plot these along the transect (blue squares in Fig. 4c). All denudation rate data are summarized in supplementary Table S1.

Within the Olympic Mountains, the topography increases steadily in height from the coast towards the center of the mountain range (Fig. 4b) where it reaches its highest elevation at Mt. Olympus (2,430 masl, at -123.7°E in Fig. 4b). Millennial timescale, cosmogenic nuclide denudation rates (Adams and Ehlers, 2018) are lowest on the western side of the mountain range (~0.2 mm/yr) and increase to maximum values of 1.2–1.4 mm/yr in the core of the mountain range (Fig. 2b, 4b). Outlier higher cosmogenic nuclide denudation rates (>1.8 mm/yr, indicated in Fig. 4c) were influenced by glaciation (Adams and Ehlers, 2018), are not representative of denudation caused by rock uplift and excluded from consideration here. Million-year timescale denudation rates from thermochronometer data (Michel et al., 2018) are highest in the core of the range (Fig. 2a). The denudation rates decrease away from the core of the range in the profile (Fig. 4c), and also in map view (Fig. 2a, S1), such that rates vary between 0.25 mm/yr at the coast to 0.9 mm/yr in the area of high topography.

The peak vertical displacement due to ETS events (Bruhat and Segall, 2016) is spatially coincident with Mt. Olympus (between -123.8°E and -123.7°E, Fig. 4f), and upward directed displacement due to ETS is observed between -124.6°E and -123°E, whereas east of -123°E the vertical displacements are zero or negative (Bruhat and Segall, 2016). The peak in ETS associated tremor activity (recorded from 2014–2018) is offset from the peak in vertical displacement and located at approximately -122.8°E. From there, the occurrence of tremor gradually decreases towards the west and no tremor activity is observed west of -124°E within our considered study area. Although the spatial extent of ETS is clearly visible today (e.g., Fig. 4f), previous studies have suggested the location over which the extent (and associated slow slip events) occur may not be constant over the seismic cycle, and can lead to megathrust earthquakes (e.g., Segall and Bradley, 2012; Wang and Tréhu, 2016). However, the spatial and temporal scales over which ETS events migrate along the subduction zone interface is not well understood.

4. Results

4.1. Reduced vertical velocity and tilt rates

Based on the methods presented in section 2.2, we find that the peak in reduced vertical velocity from GPS observations (solid green line in Fig. 4e) is located between -123.8°E and -123.6°E, close to the location of Mt. Olympus. Only the western region of the peninsula between -124.6°E and -123.6°E has positive (upward) reduced vertical velocities, with maximum rates of 1±0.4 mm/yr; the remainder of the reduced velocities are near zero or slightly negative. There are several caveats associated with elastic corrections to GPS data that are addressed in the discussion section. However, we highlight here that regardless of how elastic deformation is corrected, the gradient in the elastic correction is very low this far from the trench (Wang et al., 2012, 2003; compare also Fig. 4d,e). Given this, even an under- or overestimation of the elastic correction would not change the observed short wavelength reduced vertical velocity anomaly.

The calculated tilt rates show paired positive and negative tilting (shaded red/blue areas, Fig. 4e), implying westward rotation of topography west of Mt. Olympus and eastward rotation of topography to the east of Mt. Olympus. These rotations produce topographic upwarping, from -124.2°E to -123.4°E, centered on the inferred transition between the enigmatic gap zone and the zone of regular ETS. If we further consider as a thought experiment the simplified case of a Newtonian viscous material, then a tilting rate is also a shear strain rate which should be proportional to the shear stress (Turcotte and Schubert, 2014). This interpretation of the tilting rate is consistent with the inversion of Bruhat and Segall (2016) indicating a peak in shear stress rate at the transition from the gap zone to the ETS domain on the Cascadian subduction interface (Fig. 4a), which decays over time and implies some mechanism of stress dissipation.

4.2. Spatial correlations between the different data sets

The compilation of the published datasets and our new reduced vertical velocity and tilting rates (Fig. 4) shows the spatial relationships among the observations, and therefore provides a synoptic view of deformation on different timescales. Coincident with the location of the highest mean elevation of the range (Fig. 4b), high denudation rates from both thermochronometry and cosmogenic nuclides are observed between -123.8°E and -123.2°E (~60 km) along the transect (Fig. 4c). High magnitudes for the GPS-derived datasets (reduced vertical velocity from this study and derived ETS-induced displacement, Fig. 4e,f) are confined to shorter wavelengths (~20-30 km) at the western edge of the high elevation/denudation region (Fig. 4e,f). In this area, the tilting of the topography also transitions from westward to eastward tilt.

5. Discussion

5.1. Scaling of subduction zone deformation processes

Individual lithospheric deformation processes are manifested at different wavelengths and provide insight into mountain building processes (e.g., Bomberger et al., 2018). Here we present an analysis of how the spatial variations in denudation and rock uplift shown in Fig. 4 could relate to different deformation processes. For example, far from the subduction trench, such as in the Olympic peninsula, elastic flexural effects are smooth over wavelengths greater than 100 kilometers, so are constant or linear at the scale of the study area shown in Figs. 1 and 2. In contrast, the deviation of geodetically-constrained rock uplift from any elastic

tectonic model represented by our reduced vertical velocity profile has a characteristic wavelength of a few tens of kilometers (Fig. 4e). These differences in wavelengths allow separation of the surface expression of local variations in the mechanics of subduction zones from uncertainties in the subduction zone geometry or coupling.

As a consequence, even though the methods applied here cannot resolve the locking depth and dip of the subduction interface, there is no elastic model that can explain the short wavelength power in the rock uplift profile shown in Fig. 4e. The topography and denudation profiles also have power at characteristic wavelengths of a few tens of kilometers. Hence, stress localization effects arising from either the heterogeneity of rate-and-state conditions on the subduction interface or of the rheology of the crust better match the observed characteristic scaling of all of the observational constraints in Fig. 4 (e.g., Bruhat and Segall, 2016; Bürgmann, 2018; Li et al., 2015). Additionally, the elastic model applied in this study was developed using only the horizontal components of sparse Cascadia GPS data from the whole margin (Wang et al., 2003). Therefore, it is not derived using the vertical components of the denser Olympic Peninsula GPS network analyzed here (Fig. 4d).

Within our study area, the topographic elevation, denudation rates, and geodetic reduced vertical velocities from the Olympic Peninsula all yield a pattern consistent with positive vertical displacements centered in the Olympic Mountains between -124°E and -123°E (Fig. 4b,c,e). Although observations of deformation and denudation are coincident in space, results indicate their characteristic wavelength appears to vary systematically with the timescale of integration. For example, the elevated topography spans approximately 100 km along the transect, the high denudation rates approximately half that distance, and the positive reduced vertical velocity only 20-30 km. The domain of the present-day reduced rock uplift lies directly above the inferred transition between the fully locked and Gap Zone parts of the CSZ and that hosting ETS, where the primary subduction interface is between 25 and 35 km depth (Fig. 4). Based on a combination of observational constraints, emerging fault mechanics results, and continuum mechanics, this zone appears to be the part of the CSZ with the most complicated behavior.

5.2. Construction of permanent topography

In the steady slip zone (top of Fig. 4), the North American and Juan de Fuca plates move past each other at the relative plate velocity. This plate motion must ultimately be accommodated through the entire subduction zone up dip to close the total tectonic velocity budget. In the ETS zone (the area where tremor is recorded between -123.8°E and -122.3°E in Fig. 4f) accumulation of stress from the steadily slipping domain below appears to interact with a nearly-constant frictional threshold, resulting in quasi-periodic slip events that propagate the plate motion up-dip to the base of a 'gap' zone. Single ETS events nucleate deep on the plate interface, and the associated tremor and slip move up-dip or along-strike the plate interface (e.g., Dragert and Wang, 2011; Wech and Creager, 2011). The location of major tremor activity can be spatially offset from the location of maximum slip (Hall et al., 2018). We also observe that the tremor occurrence decreases up dip along the plate interface, and that the maximum vertical displacement due to ETS occurs close to the transition from the ETS zone to the gap zone (Fig. 4f). The elastic nature of the ETS displacement (e.g., Bartlow et al., 2011) and the fact that our other proxies are reported as rates makes a direct comparison of the ETS data with our other reported proxies difficult. This is because the short observational timescale and enigmatic nature of ETS events does not allow for the robust calculation of rates from them. We therefore refrain from doing so.

The mechanism of slip transfer through the gap zone is not well understood, but at least some of the tectonic stress must propagate through the gap to the base of the locked domain to eventually be released coseismically (Segall and Bradley, 2012). The steep slip gradient in the ETS-to-locked transition characterized by Bruhat and Segall (2016) implies interseismic stress concentration in this area, at depths of 20 – 35 km. At Cascadia, temperatures between 300 – 500 °C are reported to occur within the crust of the overriding plate at depths of 20 – 40 km (Gao and Wang, 2017; Peacock et al., 2011). Furthermore, previous work has indicated accreted sediment is present here (Calvert et al., 2011). At these depths and temperatures, continental lower crust is inferred to be ductile (Burov, 2011). Under these conditions, stresses persisting throughout the interseismic period are likely to induce visco-plastic, rather than elastic, deformation in the crust. If true, then such deformation near the subduction zone interface would be consistent with our observations of upwarping in the interseismic interval and the excitation of unrecoverable 'permanent' topography. Furthermore, visco-plastic deformation at this depth would dissipate some of the tectonic stress as required by models of negative shear stress rate (Bruhat and Segall, 2016). This interpretation is supported by Wang et al. (2012) and Li et al. (2015), who also calculated that interseismic viscous deformation excited by the accumulation of tectonic stresses below the locked part of subduction zones would not all be recovered coseismically and could reduce the elastic potential energy of subduction megathrusts.

In addition, the secular tilting we observe and interpret as arising from crustal, visco-plastic deformation above the subduction interface is also consistent with the persistent topography observed today. This interpretation is supported by the spatial correlation between tilting rate, elevated topography and high rates of denudation at the surface. More specifically, in the Olympic Mountains, we observe that the maximum denudation rates both from thermochronometry and cosmogenic nuclides are spatially correlated only with the positive reduced vertical velocities and the paired positive and negative tilting rates indicative of upwarping (Fig. 4b,c,e).

5.3. Caveats and broader implications

There are several caveats associated with this study that warrant discussion. Some of the items mentioned below can potentially be addressed in future work. First it is important to bear in mind that significant changes occur along strike of the Cascadia subduction zone, including slab dip (Hayes et al., 2018; McCrory et al., 2012), the width of the locked zone (e.g., Fig. 1a), the distribution of episodic tremor and slip (Wells et al., 2017), and lateral variations in topography and denudation rate (Bodmer et al., 2020). Compared to areas further north and south, the Olympic Mountains are an area of flat slab subduction. The resulting slab geometry results in localized exhumation (Bendick and Ehlers, 2014; Koptev et al., 2019; Michel et al., 2018; Nettesheim et al., 2018). We suggest that our proposed change in subduction zone properties and the visco-plastic deformation is distinct, persistent, and well-measured at the latitude of the Olympic Mountains compared to other areas of the subduction zone. This might be due to three factors including: the slab geometry below the Olympic Mountains; the presence of underplated sediment at depth (Calvert et al., 2011); or the stability of the different accommodation mechanisms on the subduction interface.

Second, we suggest that much of the reduced vertical velocity (the difference between the GPS uplift rate and the predicted elastic component from the inter-seismic elastic locking model) is manifested as permanent deformation leading to the construction

and maintenance of topography. This interpretation is sensitive to the rheology and architecture of the study domain, such that variations in the depth, viscosity, and equations of state for inelastic materials would change both the scaling and the total strain budget of the surface deformation (e.g., Koptev et al., 2019). For example, highly non-linear viscous models should be expected to localize deformation more than Newtonian models. Unfortunately, a more detailed modeling approach (e.g., visco-elastic, plastic) that goes beyond the elastic correction applied here is unlikely to be fruitful because of the introduction of additional, poorly or unconstrained, free parameters in coupled thermo-mechanical simulations.

Third, the geodetic and geomorphic constraints presented here are sensitive to different time scales. More specifically, the geodetic data record processes over tens of years whereas the geomorphic data are sensitive to processes active over thousands or hundreds of thousands of years. Therefore, we cannot determine whether the reduced vertical velocities represent a steady state regime that builds the topography or whether they represent just a snapshot of vertical velocities that change in magnitude, scaling, and location within and between seismic cycles. Hence, our assumption that the reduced vertical velocity is steady-state and provides all of the deformation stored as topography is only a bounding constraint. However, the similarity in the magnitudes, spatial locations, and characteristic scaling of geodetic and geomorphic rates suggests that the natural example of Cascadia is likely to be close to the limit in which most of the reduced vertical rock uplift contributes to orogenesis.

Furthermore, the present-day interseismic locking geometry may itself be time-dependent. For example, Bruhat and Segall (2017) suggested that the creeping zone of the subduction interface (comprised of the gap zone and the zone of ETS) propagates up-dip over time during the interseismic period. While their interpretation is not unique, we find that a temporal migration of where permanent deformation occurs on the subduction zone interface is consistent with our results. We see that the present-day maximum in the reduced vertical velocity (Fig. 4e) is located at the up-dip (westward) limit of the ETS zone and maximum in the topography. However, the high topography of the Olympic Mountains extends >100 km to the east (Fig. 4b) of the maximum in reduced vertical GPS velocities. Thus, construction of all the high topography in the Olympic Mountains would require that permanent deformation at the subduction zone (as suggested here) migrates through time along the subduction zone interface from east to west, consistent with the up-dip migration of the creeping zone through time proposed by Bruhat and Segall (2017). In addition, recent work highlighted that the maximum elevation of topography at convergent plate margins depends on the shear force on the plate interface (Dielforder et al., 2020; Dielforder and Hampel, 2021). A higher shear force is expected in the creeping zone (compared to the freely slipping zone below). Given the width of the high-topography area a spatial migration of the creeping zone over the seismic zone seems likely.

Fourth, climatic perturbations on million-year timescales like the onset of the Northern Hemisphere glaciation also affect the comparison and spatial correlation between the different datasets, because the present-day topography of the Olympic Mountains (as shown in Fig. 4b) is modified by Plio-Pleistocene glaciation (Adams and Ehlers, 2017; Montgomery, 2002). Michel et al. (2018) suggested an increase in denudation rates with the onset of the Plio-Pleistocene glaciation, modifying the topography such that the pre-glacial, maximum elevation of the mountain range was higher, and that more elevated topography was present to the west of Mt. Olympus. Hence, the initial (pre-glacial) topographic signal is different from what we observe today, and today's topographic signal is the combined effect of the long-term tectonic processes and short-term modifications by climatic perturbations. But, if the topographic gradient was indeed steeper and the highest topography focused in the area around Mt. Olympus, then this would suggest an even stronger spatial correlation between the areas of highest topography and the area where we today observe the highest reduced vertical velocity (Fig. 4e).

Lastly, the permanent plastic deformation expressed as topography and advection of rocks represents the total deformation after the full earthquake cycle is completed, and includes the (yet unobserved) co-seismic phase. Given this, our estimate of permanent deformation, like our estimates of rock uplift from geodesy, has a degree of unquantifiable uncertainty to it. We currently don't know where we are within the seismic cycle, aside from that at the CSZ margin, mega-earthquakes have average recurrence intervals of five centuries, with the last mega-earthquake having occurred in AD 1700 (Wang and Tréhu, 2016).

5.4. Comparison to other settings and geologic processes

The interpretations presented here are similar to previous findings identified along 2,000 km of the central Andean coast where lower parts of the subduction zone interface are segmented over geologic timescales and moderate earthquakes in the conditionally stable domain lead to the long-term construction of topography (Madella and Ehlers, 2021; Melnick, 2016). However, subduction of the Nazca Plate under South America has resulted in an subduction-erosion tectonic setting for at least the last 20 Ma, in contrast to the accretionary setting observed in Cascadia (Allmendinger and González, 2010; Armijo et al., 2015; Lamb and Davis, 2003; Martinod et al., 2016; Oncken et al., 2003; von Huene and Ranero, 2003). This suggests that regardless of the tectonic setting (erosive or accretionary), deep seated processes near the subduction zone interface are responsible for surface uplift over geologic timescales.

The geologic structures forming at the subduction zone interface and responsible for long-term surface uplift most likely include duplex structures that result in thickening of the upper plate and the possible transfer of lower plate material into the upper plate during individual duplex formation. This interpretation is supported by seismic profiles across the Cascadia fore-arc that suggest duplex formation (e.g., Calvert et al., 2006). Furthermore, underplating of subducted material has been documented in accretionary complexes elsewhere (e.g., Kimura et al., 1996; Meneghini and Moore, 2007; Onishi et al., 2001; Schmidt and Platt, 2018). It is likely that deformation related to the underplating of material and duplex formation also contributes to rock uplift and formation of topography.

6. Conclusions

We find that the patterns of denudation rates obtained from cosmogenic nuclides and thermochronometry in the Olympic Mountains are similar. This similarity suggests that most long-term (permanent) deformation occurs in the center of the mountain range, where topography is highest. The permanent deformation recorded by topography and dating techniques partially aligns with a peak in reduced vertical velocity observed using geodetic methods, as well as with high rates of surface tilting. Based on comparisons to previous studies of subduction interface processes, we conclude that the coincidence of patterns in the denudation rates and GPS data suggest that localized stresses on the plate interface of the Cascadian Subduction Zone excite viscous deformation in the accreted sediments of the lower crust. This deformation may dissipate some of the tectonic shear stress in the enigmatic 'gap' zone, generate permanent topography through crustal thickening

and duplex formation, enhance denudation rates, and perhaps limit the maximum moment of Cascadian megaquakes.

The findings presented here have broad implications for understanding the relationship between orogenesis and the seismic cycle. For example, previous studies have highlighted that comparisons between methods integrating over different timescales contain discrepancies (e.g., Friedrich et al., 2003; Niemi and Clark, 2018; Penserini et al., 2017; Stock et al., 2009; Huntington et al., 2007). This could in part be due to short timescale observations (e.g., geodetic) recording both elastic and inelastic components, whereas observations over longer integration timescales only record inelastic deformation. Our study shows that the removal of the elastic component by forward modeling holds promise for identifying a permanent component of deformation contained in a GPS-determined rock uplift rate. In our case, geodetic reduced vertical rock uplift rates are similar in magnitude to the observed denudation rates and around 1 mm/yr. They differ mainly in their characteristic length scales, with the length scale of uplift decreasing with decreasing integration duration. For example, as previously mentioned, both the pattern of topography and denudation rates occur over longer wavelengths than the positive reduced vertical GPS uplift anomaly. With less than one seismic cycle captured in the geodetic observations, we cannot determine whether this implies a systematic trenchward propagation of the most active topography-forming region of deformation.

Our uncertainty stems from possible spatial variations in the location in the visco-plastic deforming region within and between seismic cycles, variations in the mechanics of the subduction interface over time, or changes in the geometry of the subduction interface over many seismic cycles. The presence of high elevation east of the positive reduced vertical velocity suggests that the geodetic pattern we observe over decadal time scales has either migrated west with time or fluctuates back and forth underneath the region of high topography (Segall and Bradley, 2012). Alternatively, the pattern is biased by the fact that the Cascadia Subduction Zone is now late in the interseismic period (Wang and Tréhu, 2016), when visco-elastic simulations predict widening of a domain of surface subsidence related to the downdip limit of the ETS zone.

CRediT authorship contribution statement

All authors have contributed to the work, approved the manuscript and agreed on its submission.

All authors were involved in planning the work. LMW and TAE are responsible for compilation of denudation and tremor data, and RB for GPS derived calculations. All authors contributed to manuscript and figure preparation.

Declaration of competing interest

The authors declare that they have no known competing financial interests or personal relationships that could have appeared to influence the work reported in this paper.

Acknowledgements

We thank Kelin Wang for generously sharing his raw elastic model calculations. We appreciate editorial handling by editor Alex Webb, and constructive reviews by John Platt and Eric Cowgill. We also acknowledge comments by Paul Segall, Onno Oncken and Alex Densmore on earlier versions of this manuscript. This study was funded by a European Research Council (ERC) consolidator grant (CoG 615703) to TAE.

Appendix A. Supplementary material

Supplementary material related to this article can be found online at https://doi.org/10.1016/j.epsl.2021.117363.

References

Adams, B.A., Ehlers, T.A., 2017. Deciphering topographic signals of glaciation and rock uplift in an active orogen: a case study from the Olympic Mountains, USA. Earth Surf. Process. Landf. 42, 1680–1692. https://doi.org/10.1002/esp.4120.

Adams, B.A., Ehlers, T.A., 2018. Tectonic controls of Holocene erosion in a glaciated orogen. Earth Surf. Dyn. 6, 595–610. https://doi.org/10.5194/esurf-6-595-2018.

Allmendinger, R.W., González, G., 2010. Invited review paper: Neogene to Quaternary tectonics of the coastal Cordillera, northern Chile. Tectonophysics 495, 93–110. https://doi.org/10.1016/j.tecto.2009.04.019.

Armijo, R., Lacassin, R., Coudurier-Curveur, A., Carrizo, D., 2015. Coupled tectonic evolution of Andean orogeny and global climate. Earth-Sci. Rev. 143, 1–35. https://doi.org/10.1016/j.earscirev.2015.01.005.

Bartlow, N.M., Miyazaki, S., Bradley, A.M., Segall, P., 2011. Space-time correlation of slip and tremor during the 2009 Cascadia slow slip event. Geophys. Res. Lett. 38. https://doi.org/10.1029/2011GL048714.

Bendick, R., Ehlers, T.A., 2014. Extreme localized exhumation at syntaxes initiated by subduction geometry. Geophys. Res. Lett. 41, 5861–5867. https://doi.org/10.1002/2014GL061026.

Bodmer, M., Toomey, D.R., Roering, J.J., Karlstrom, L., 2020. Asthenospheric buoyancy and the origin of high-relief topography along the Cascadia forearc. Earth Planet. Sci. Lett. 531, 115965. https://doi.org/10.1016/j.epsl.2019.115965.

Bomberger, C., Bendick, R., Flesch, L., Ehlers, T.A., 2018. Spatial scales in topography and strain rate magnitude in the western United States. J. Geophys. Res., Solid Earth. https://doi.org/10.1029/2018JB016135.

Brandon, M.T., Roden-Tice, M.K., Garver, J.I., 1998. Late Cenozoic exhumation of the Cascadia accretionary wedge in the Olympic Mountains, northwest Washington State. Geol. Soc. Am. Bull. 110, 985–1009. https://doi.org/10.1130/0016-7606(1998)110<0985:LCEOTC>2.3.CO;2.

Bruhat, L., Segall, P., 2016. Coupling on the northern Cascadia subduction zone from geodetic measurements and physics-based models. J. Geophys. Res., Solid Earth 121, 8297–8314. https://doi.org/10.1002/2016JB013267.

Bruhat, L., Segall, P., 2017. Deformation rates in northern Cascadia consistent with slow updip propagation of deep interseismic creep. Geophys. J. Int. 211, 427–449. https://doi.org/10.1093/gji/ggx317.

Burgette, R.J., Weldon, R.J., Schmidt, D.A., 2009. Interseismic uplift rates for western Oregon and along-strike variation in locking on the Cascadia subduction zone. J. Geophys. Res., Solid Earth 114. https://doi.org/10.1029/2008JB005679.

Bürgmann, R., 2018. The geophysics, geology and mechanics of slow fault slip. Earth Planet. Sci. Lett. 495, 112–134. https://doi.org/10.1016/j.epsl.2018.04.062.

Burov, E.B., 2011. Rheology and strength of the lithosphere. Mar. Pet. Geol. 28, 1402–1443. https://doi.org/10.1016/j.marpetgeo.2011.05.008.

Calvert, A.J., Preston, L.A., Farahbod, A.M., 2011. Sedimentary underplating at the Cascadia mantle-wedge corner revealed by seismic imaging. Nat. Geosci. 4, 545–548. https://doi.org/10.1038/ngeo1195.

Calvert, A.J., Ramachandran, K., Kao, H., Fisher, M.A., 2006. Local thickening of the Cascadia forearc crust and the origin of seismic reflectors in the uppermost mantle. In: Seismic Probing of Continents and Their Margins, 11th International Symposium on Deep Seismic Profiling of the Continents and Their Margins. Tectonophysics 420, 175–188. https://doi.org/10.1016/j.tecto.2006.01.021.

Dielforder, A., Hampel, A., 2021. Force-balance analysis of stress changes during the subduction-collision transition and implications for the rise of mountain belts. J. Geophys. Res., Solid Earth 126. https://doi.org/10.1029/2020JB020914.

Dielforder, A., Hetzel, R., Oncken, O., 2020. Megathrust shear force controls mountain height at convergent plate margins. Nature 582, 225–229. https://doi.org/10.1038/s41586-020-2340-7.

Dragert, H., Wang, K., 2011. Temporal evolution of an episodic tremor and slip event along the northern Cascadia margin. J. Geophys. Res. 116. https://doi.org/10.1029/2011JB008609.

Ellis, M.A., Densmore, A.L., Anderson, R.S., 1999. Development of mountainous topography in the Basin Ranges, USA. Basin Res. 11, 21–41. https://doi.org/10.1046/j.1365-2117.1999.00087.x.

England, P., Molnar, P., 1990. Surface uplift, uplift of rocks, and exhumation of rocks. Geology 18, 1173–1177. https://doi.org/10.1130/0091-7613(1990)018<1173:SUUORA>2.3.CO;2.

Friedrich, A.M., Wernicke, B.P., Niemi, N.A., Bennett, R.A., Davis, J.L., 2003. Comparison of geodetic and geologic data from the Wasatch region, Utah, and implications for the spectral character of Earth deformation at periods of 10 to 10 million years. J. Geophys. Res., Solid Earth 108. https://doi.org/10.1029/2001JB000682.

Fu, Y., Argus, D.F., Landerer, F.W., 2015. GPS as an independent measurement to estimate terrestrial water storage variations in Washington and Oregon. J. Geophys. Res., Solid Earth 120, 552–566. https://doi.org/10.1002/2014JB011415.

Gao, X., Wang, K., 2017. Rheological separation of the megathrust seismogenic zone and episodic tremor and slip. Nature 543, 416–419. https://doi.org/10.1038/nature21389.

Hall, K., Houston, H., Schmidt, D., 2018. Spatial comparisons of tremor and slow slip as a constraint on fault strength in the northern Cascadia subduction zone. Geochem. Geophys. Geosyst. 19, 2706–2718. https://doi.org/10.1029/2018GC007694.

Hawthorne, J.C., Rubin, A.M., 2013. Short-time scale correlation between slow slip and tremor in Cascadia. J. Geophys. Res., Solid Earth 118, 1316–1329. https://doi.org/10.1002/jgrb.50103.

Hayes, G.P., Moore, G.L., Portner, D.E., Hearne, M., Flamme, H., Furtney, M., Smoczyk, G.M., 2018. Slab2, a comprehensive subduction zone geometry model. Science 362, 58–61. https://doi.org/10.1126/science.aat4723.

Herring, T.A., Melbourne, T.I., Murray, M.H., Floyd, M.A., Szeliga, W.M., King, R.W., Phillips, D.A., Puskas, C.M., Santillan, M., Wang, L., 2016. Plate boundary observatory and related networks: GPS data analysis methods and geodetic products. Rev. Geophys. 54, 759–808. https://doi.org/10.1002/2016RG000529.

Huntington, K.W., Ehlers, T.A., Hodges, K.V., Whipp, D.M., 2007. Topography, exhumation pathway, age uncertainties, and the interpretation of thermochronometer data. Tectonics 26. https://doi.org/10.1029/2007TC002108.

Hyndman, R.D., 2013. Downdip landward limit of Cascadia great earthquake rupture. J. Geophys. Res., Solid Earth 118, 5530–5549. https://doi.org/10.1002/jgrb.50390.

Hyndman, R.D., Wang, K., 1993. Thermal constraints on the zone of major thrust earthquake failure: the Cascadia subduction zone. J. Geophys. Res., Solid Earth 98, 2039–2060. https://doi.org/10.1029/92JB02279.

James, T.S., Gowan, E.J., Wada, I., Wang, K., 2009. Viscosity of the asthenosphere from glacial isostatic adjustment and subduction dynamics at the northern Cascadia subduction zone, British Columbia, Canada. J. Geophys. Res. 114, B04405. https://doi.org/10.1029/2008JB006077.

Kelsey, H.M., Engebretson, D.C., Mitchell, C.E., Ticknor, R.L., 1994. Topographic form of the coast ranges of the Cascadia margin in relation to coastal uplift rates and plate subduction. J. Geophys. Res., Solid Earth 99, 12245–12255. https://doi.org/10.1029/93JB03236.

Kimura, G., Maruyama, S., Isozaki, Y., Terabayashi, M., 1996. Well-preserved underplating structure of the jadeitized Franciscan complex, Pacheco Pass, California. Geology 24, 75–78. https://doi.org/10.1130/0091-7613(1996)024<0075:WPUSOT>2.3.CO;2.

Koptev, A., Ehlers, T.A., Nettesheim, M., Whipp, D., 2019. Response of a rheologically stratified lithosphere to subduction of an indenter-shaped plate: insights into localized exhumation at orogen syntaxes. Tectonics. https://doi.org/10.1029/2018TC005455.

Krogstad, R.D., Schmidt, D.A., Weldon, R.J., Burgette, R.J., 2016. Constraints on accumulated strain near the ETS zone along Cascadia. Earth Planet. Sci. Lett. 439, 109–116. https://doi.org/10.1016/j.epsl.2016.01.033.

Lamb, S., Davis, P., 2003. Cenozoic climate change as a possible cause for the rise of the Andes. Nature 425, 792–797. https://doi.org/10.1038/nature02049.

Lay, T., Kanamori, H., Ammon, C.J., Koper, K.D., Hutko, A.R., Ye, L., Yue, H., Rushing, T.M., 2012. Depth-varying rupture properties of subduction zone megathrust faults. J. Geophys. Res. 117, B04311. https://doi.org/10.1029/2011JB009133.

Li, S., Moreno, M., Bedford, J., Rosenau, M., Oncken, O., 2015. Revisiting viscoelastic effects on interseismic deformation and locking degree: a case study of the Peru-North Chile subduction zone. J. Geophys. Res., Solid Earth 120, 4522–4538. https://doi.org/10.1002/2015JB011903.

Li, S., Wang, K., Wang, Y., Jiang, Y., Dosso, S.E., 2018. Geodetically inferred locking state of the Cascadia megathrust based on a viscoelastic Earth model. J. Geophys. Res., Solid Earth 123, 8056–8072. https://doi.org/10.1029/2018JB015620.

Madella, A., Ehlers, T.A., 2021. Contribution of background seismicity to forearc uplift. Nat. Geosci. 14, 620–625. https://doi.org/10.1038/s41561-021-00779-0.

Mansinha, L., Smylie, D.E., 1971. The displacement fields of inclined faults. Bull. Seismol. Soc. Am. 61, 1433–1440.

Martinod, J., Regard, V., Letourmy, Y., Henry, H., Hassani, R., Baratchart, S., Carretier, S., 2016. How do subduction processes contribute to forearc Andean uplift? Insights from numerical models. J. Geodyn. 96, 6–18. https://doi.org/10.1016/j.jog.2015.04.001.

McCaffrey, R., 2009. Time-dependent inversion of three-component continuous GPS for steady and transient sources in northern Cascadia. Geophys. Res. Lett. 36, L07304. https://doi.org/10.1029/2008GL036784.

McCaffrey, R., Qamar, A.I., King, R.W., Wells, R., Khazaradze, G., Williams, C.A., Stevens, C.W., Vollick, J.J., Zwick, P.C., 2007. Fault locking, block rotation and crustal deformation in the Pacific northwest. Geophys. J. Int. 169, 1315–1340. https://doi.org/10.1111/j.1365-246X.2007.03371.x.

McCrory, P.A., Blair, J.L., Waldhauser, F., Oppenheimer, D.H., 2012. Juan de Fuca slab geometry and its relation to Wadati-Benioff zone seismicity. J. Geophys. Res., Solid Earth 117, B09306. https://doi.org/10.1029/2012JB009407.

Melnick, D., 2016. Rise of the central Andean coast by earthquakes straddling the Moho. Nat. Geosci. 9, 401–407. https://doi.org/10.1038/ngeo2683.

Meneghini, F., Moore, J.C., 2007. Deformation and hydrofracture in a subduction thrust at seismogenic depths: the Rodeo Cove thrust zone, Marin Headlands, California. Geol. Soc. Am. Bull. 119, 174–183. https://doi.org/10.1130/B25807.1.

Michel, L., Ehlers, T.A., Glotzbach, C., Adams, B.A., Stübner, K., 2018. Tectonic and glacial contributions to focused exhumation in the Olympic Mountains, Washington, USA. Geology 46, 491–494. https://doi.org/10.1130/G39881.1.

Michel, L., Glotzbach, C., Falkowski, S., Adams, B.A., Ehlers, T.A., 2019. How steady are steady-state mountain belts? A reexamination of the Olympic Mountains (Washington state, USA). Earth Surf. Dyn. 7, 275–299. https://doi.org/10.5194/esurf-7-275-2019.

Montgomery, D.R., 2002. Valley formation by fluvial and glacial erosion. Geology 30, 1047–1050. https://doi.org/10.1130/0091-7613(2002)030<1047:VFBFAG>2.0.CO;2.

Nettesheim, M., Ehlers, T.A., Whipp, D.M., Koptev, A., 2018. The influence of upper-plate advance and erosion on overriding plate deformation in orogen syntaxes. Solid Earth 9, 1207–1224. https://doi.org/10.5194/se-9-1207-2018.

Niemi, N.A., Clark, M.K., 2018. Long-term exhumation rates exceed paleoseismic slip rates in the central Santa Monica Mountains, Los Angeles County, California. Geology 46, 63–66. https://doi.org/10.1130/G39388.1.

Okada, Y., 1985. Surface deformation due to shear and tensile faults in a half-space. Bull. Seismol. Soc. Am. 75, 1135–1154.

Oncken, O., Asch, G., Haberland, C., Metchie, J., Sobolev, S., Stiller, M., Yuan, X., Brasse, H., Buske, S., Giese, P., Görze, H.-J., Lueth, S., Scheuber, E., Shapiro, S., Wigger, P., Yoon, M.-K., Bravo, P., Vieytes, H., Chong, G., Gonzales, G., Wilke, H.-G., Lüschen, E., Martinez, E., Rössling, R., Ricaldi, E., Rietbrock, A., 2003. Seismic imaging of a convergent continental margin and plateau in the central Andes (Andean Continental Research Project 1996 (ANCORP'96)). J. Geophys. Res., Solid Earth 108. https://doi.org/10.1029/2002JB001771.

Onishi, C.T., Kimura, G., Hashimoto, Y., Ikehara-Ohmori, K., Watanabe, T., 2001. Deformation history of tectonic melange and its relationship to the underplating process and relative plate motion: an example from the deeply buried Shimanto Belt, SW Japan. Tectonics 20, 376–393. https://doi.org/10.1029/1999TC001154.

Peacock, S.M., Christensen, N.I., Bostock, M.G., Audet, P., 2011. High pore pressures and porosity at 35 km depth in the Cascadia subduction zone. Geology 39, 471–474. https://doi.org/10.1130/G31649.1.

Penserini, B.D., Roering, J.J., Streig, A., 2017. A morphologic proxy for debris flow erosion with application to the earthquake deformation cycle, Cascadia subduction zone, USA. Geomorphology 282, 150–161. https://doi.org/10.1016/j.geomorph.2017.01.018.

Rogers, G., Dragert, H., 2003. Episodic tremor and slip on the Cascadia subduction zone: the chatter of silent slip. Science 300, 1942–1943. https://doi.org/10.1126/science.1084783.

Schmidt, W.L., Platt, J.P., 2018. Subduction, accretion, and exhumation of coherent Franciscan blueschist-facies rocks, northern Coast Ranges, California. Lithosphere 10, 301–326. https://doi.org/10.1130/L697.1.

Segall, P., Bradley, A.M., 2012. Slow-slip evolves into megathrust earthquakes in 2D numerical simulations: slow-slip and Megathrust quakes. Geophys. Res. Lett. 39. https://doi.org/10.1029/2012GL052811.

Simpson, G., 2015. Accumulation of permanent deformation during earthquake cycles on reverse faults. J. Geophys. Res., Solid Earth 120, 1958–1974. https://doi.org/10.1002/2014JB011442.

Stock, G.M., Frankel, K.L., Ehlers, T.A., Schaller, M., Briggs, S.M., Finkel, R.C., 2009. Spatial and temporal variations in denudation of the Wasatch Mountains, Utah, USA. Lithosphere 1, 34–40. https://doi.org/10.1130/L15.1.

Szeliga, W., Melbourne, T., Santillan, M., Miller, M., 2008. GPS constraints on 34 slow slip events within the Cascadia subduction zone, 1997–2005. J. Geophys. Res. 113. https://doi.org/10.1029/2007JB004948.

Turcotte, D.L., Schubert, G., 2014. Geodynamics. Cambridge University Press.

von Huene, R., Ranero, C.R., 2003. Subduction erosion and basal friction along the sediment-starved convergent margin off Antofagasta, Chile: subduction erosion, sediment-starved margin. J. Geophys. Res., Solid Earth 108. https://doi.org/10.1029/2001JB001569.

Wang, K., Hu, Y., He, J., 2012. Deformation cycles of subduction earthquakes in a viscoelastic Earth. Nature 484, 327–332. https://doi.org/10.1038/nature11032.

Wang, K., Tréhu, A.M., 2016. Invited review paper: some outstanding issues in the study of great megathrust earthquakes—the Cascadia example. J. Geodyn. 98, 1–18. https://doi.org/10.1016/j.jog.2016.03.010.

Wang, K., Wells, R., Mazzotti, S., Hyndman, R.D., Sagiya, T., 2003. A revised dislocation model of interseismic deformation of the Cascadia subduction zone. J. Geophys. Res., Solid Earth 108. https://doi.org/10.1029/2001JB001227.

Wech, A.G., Bartlow, N.M., 2014. Slip rate and tremor genesis in Cascadia. Geophys. Res. Lett. 41, 392–398. https://doi.org/10.1002/2013GL058607.

Wech, A.G., Creager, K.C., 2011. A continuum of stress, strength and slip in the Cascadia subduction zone. Nat. Geosci. 4, 624–628. https://doi.org/10.1038/ngeo1215.

Wells, R.E., Blakely, R.J., Wech, A.G., McCrory, P.A., Michael, A., 2017. Cascadia subduction tremor muted by crustal faults. Geology 45, 515–518. https://doi.org/10.1130/G38835.1.

Yousefi, M., Milne, G., Li, S., Wang, K., Bartholet, A., 2020. Constraining interseismic deformation of the Cascadia subduction zone: new insights from estimates of vertical land motion over different timescales. J. Geophys. Res., Solid Earth 125. https://doi.org/10.1029/2019JB018248.